Rock Mechanics Bulletin 5 (2026) 100254

Contents lists available at ScienceDirect

Rock Mechanics Bulletin

journal homepage: www.keaipublishing.com/en/journals/rock-mechanics-bulletin

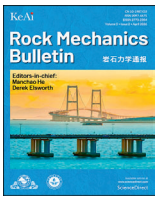

Full Length Article

Mechanical behavior and strength model of anchored mortar-rock composite under triaxial compression

Minzhen Zhang[a,b], Yanlin Zhao[a,*], Wenyu Tang[a], Rui Luo[a], Tianyao Li[a], Ximing Luo[a]

[a] School of Resources, Environment and Safety Engineering, Hunan University of Science and Technology, Xiangtan, Hunan, 411201, China
[b] School of Civil and Resource Engineering, University of Science and Technology Beijing, Beijing, 100083, China

ARTICLE INFO

Keywords:
Mortar-rock interface
Triaxial compression
Bolt inclination angle
Mechanical properties
Strength model

ABSTRACT

Anchor-shotcrete support has been widely applied in underground rock mass engineering globally, where the anchoring of bolts plays a crucial role in stabilizing the mortar-rock interface. In this study, triaxial compression tests were conducted on anchored mortar-rock composite specimens under varying confining pressures, and the failure mechanisms of the anchored mortar-rock composites were investigated using acoustic emission (AE) and three-dimensional morphology scanning techniques. The results indicate that the bolt inclination angle significantly influences the plastic deformation and compressive strength of the mortar-rock composites during triaxial compression tests. The composite specimens with a bolt inclination angle of 90° between the bolt and the mortar-rock interface exhibited the optimal load-bearing performance. As the confining pressure increased, the anchored mortar-rock composites primarily underwent plastic deformation, reducing the property differences caused by varying bolt angles. The bolt angles led to four distinct failure modes in the mortar-rock composites. The acoustic emission (AE) signals during the tests demonstrated that the mortar-rock composites with a bolt inclination angle of 90° exhibited the highest stability. Additionally, the study revealed that the morphological parameters of the mortar-rock interface varied positively with the bolt inclination angle. Finally, a strength model for the anchored mortar-rock composites under triaxial compression was derived. The reliability of the strength model was validated by comparing the experimental results with the model predictions under four different confining pressures.

1. Introduction

In underground rock mass engineering, the extensive application of anchor-shotcrete support has led to the emergence of numerous mortar-bolt-rock composite structures (Terron-Almenara et al., 2025; Yang et al., 2024; Zheng et al., 2025). These structures significantly enhance the stability of rock masses through the interaction between bolts and the mortar-rock interface, serving as a crucial safeguard for engineering safety under complex geological conditions. The bolt inclination angle of bolts, as one of the key design parameters (Xue et al., 2025), directly influences the mechanical properties and failure modes of the mortar-bolt-rock composites. However, the mechanisms by which the bolt inclination angle affects the mechanical behavior of mortar-rock composites under triaxial compression have not yet been fully studied, particularly regarding their failure characteristics and strength models under complex stress states, which require further exploration.

Currently, numerous scholars have conducted extensive research on the shear and compression behaviors of mortar-rock composites, encompassing various mortar-rock materials (Wang et al., 2020; Yuan et al., 2024; Zhang et al.), different interface morphologies (Chen et al., 2023; Renaud et al., 2021), varying interface inclination angles (Liu et al., 2025; Selçuk and Aşma, 2019; Zhang et al., 2024b), and different normal stresses (Liao et al., 2025; Zhao et al., 2022) among other factors (Zang and Wang, 2026). These elements can significantly influence the mechanical properties of mortar-rock composite materials. Correspondingly, research has also been carried out on the mechanical properties of anchored materials, taking into account factors such as bolt length (Zhang et al., 2024a), bolt angle (Feng et al., 2025; Li and Liu, 2019), bolt pre-stress (Gregor et al., 2023), loading methods (Pinazzi et al., 2020), and the matrix material of the bolt (Fu et al., 2024). Wu et al. (2020) performed uniaxial compression tests on anchored composite materials and discovered that the composite anchored materials

* Corresponding author.
E-mail address: zhangyangmz@xs.ustb.edu.cn (M. Zhang).
Peer review under the responsibility of Chinese Society for Rock Mechanics & Engineering.

https://doi.org/10.1016/j.rockmb.2025.100254
Received 15 April 2025; Received in revised form 27 July 2025; Accepted 30 August 2025
Available online 17 September 2025

exhibit favorable post-peak mechanical properties.

In most engineering scenarios, materials are subjected to triaxial stress conditions. Weilv et al. (2021) conducted triaxial compression tests on cemented paste backfill-rock composite materials with two interface angles and three cement contents, proposing a bilinear peak strength envelope for the paste backfill-rock composite materials. Wang et al. (2025) carried out seepage-stress coupling experiments on sandstone-concrete composite specimens with different contact surface inclination angles, discovering that increasing confining pressure and decreasing water seepage pressure enhanced the deformation and failure resistance of the composite, while also reducing its brittleness. Compression tests on anchored composite materials under triaxial conditions revealed that the peak axial strain and triaxial compressive strength of the anchored composite materials decreased as the interface angle increased (Yu et al., 2021).

The structural instability of composite materials is predominantly attributed to interfacial sliding at the material interfaces. This study systematically investigates the mechanical behavior of anchored mortar-rock composites through a series of triaxial compression tests performed under four distinct confining pressure regimes, with controlled variations of interfacial bolt angles. A comprehensive analysis was conducted to characterize the stress-strain response, failure mechanisms, and damage evolution patterns. Concurrently, real-time acoustic emission monitoring revealed distinct energy release characteristics corresponding to different failure stages. Post-failure interfacial morphological parameters were quantitatively evaluated using 3D laser scanning, while the developed strength prediction model demonstrated strong predictive capability across multi-scale experimental conditions. These findings provide critical insights for optimizing composite material design in geotechnical engineering applications.

2. Test method

2.1. Preparation of anchored mortar-rock composite specimens

The research object was green sandstone, and the collected rock samples were processed into standard cylindrical specimens with a diameter of 50 mm and a height of 100 mm. The standard cylindrical green sandstone samples were cut using wire cutting, with the cutting surface at a 60° angle to the horizontal plane. The cutting surface exhibited regular serrations, with an undulating angle of 45° (Shan et al., 2025). Based on existing design experience for bolt inclination angles, six groups of boreholes with different inclination angles were drilled at the center of the specimen's cutting surface. The angles between the borehole axis and the structural plane were 30°, 60°, 90°, 120°, 135°, and 150° (Chen and Li, 2015; Maiolino and Pellet, 2015; Zhang et al., 2023). The aperture size was 4 mm. After processing, the specimens were bisected into two symmetrical parts. Threaded bolts with a diameter of 3 mm and a length of 50 mm were embedded into the through holes. The tensile strength of the bolts was 515 MPa, and the yield strength was 205 MPa (Wu et al., 2020). Half of each bolt was buried into the borehole and fixed, as shown in Fig. 1a. The specimens were then placed in standard cylindrical molds, and the through-hole gaps were filled with cement mortar. The cement mortar was poured from the top and fully vibrated to remove air bubbles, as shown in Fig. 1b. After pouring, the specimens were formed into Φ50 mm × 100 mm anchored mortar-rock joint specimens. Following the initial setting of the mortar, the specimens were removed from the molds and placed in a standard constant temperature and humidity curing chamber, set at 25 °C with a relative humidity of 90%, and cured for 28 days. After curing, the surfaces of the specimens were polished, as shown in Fig. 1c. The schematic diagram of the finished specimen is shown in Fig. 1d. The mortar was composed of ordinary Portland cement with a grade of 52.5, fine sand with a particle size of less than 0.5 mm, and a weight ratio of cement, sand, and water of 2:1:0.6. Four specimens were prepared for each bolt angle, totaling 24 anchored mortar-rock composite specimens, along with four specimens without anchor bolts as a control group.

2.2. Mechanical test and acoustic emission monitoring

Triaxial compression tests were conducted on mortar-rock composite specimens with different bolt inclination angles using the MTS815 rock mechanics testing system in the Rock Mechanics Laboratory of Hunan University of Science and Technology. The axial pressure and confining pressure of the system are independent servo control systems, as shown in Fig. 2a. The specific test operation process is as follows: ①Install the specimen and the circumferential and axial extensometer on the specimen, put down the three-axis cavity, and fill the cavity with hydraulic oil; ②The confining pressure was loaded to the set value with a loading rate of 0.05 MP/s; ③The specimen was loaded axially at a loading rate of 0.05 mm/min until the specimen was destroyed and the residual strength was obtained.

At the same time, the PCI-2 acoustic emission system is used to

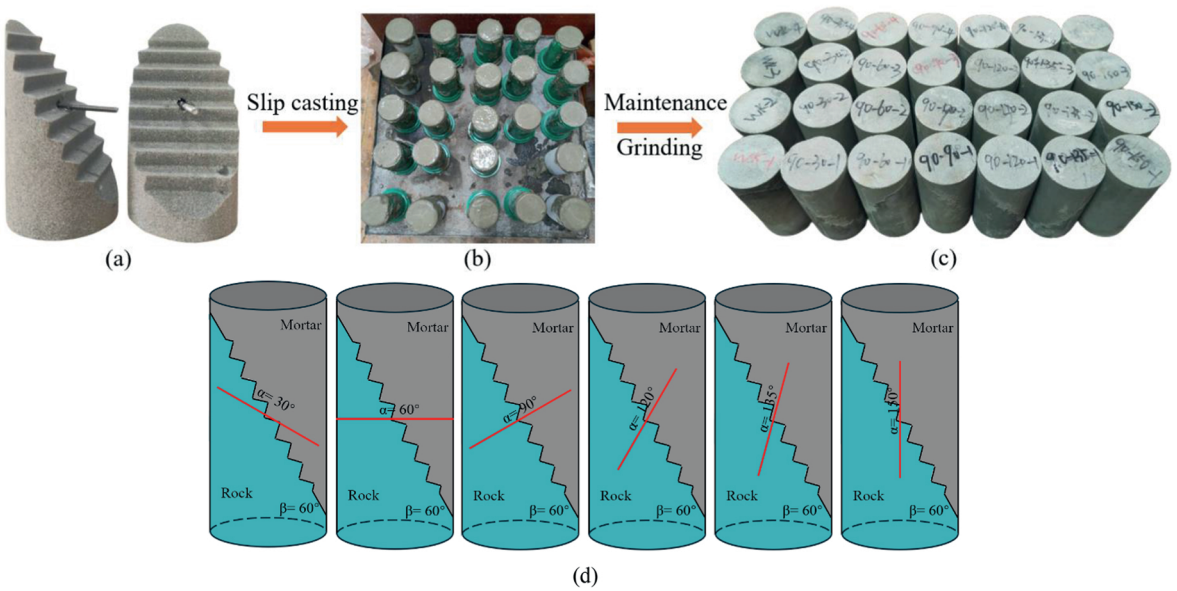

Fig. 1. Sample making schematic diagram.

(a)MTS815 rock mechanics test system (b) PCI-2 acoustic emission monitoring system

Fig. 2. Testing equipment.

monitor the acoustic emission signal of the specimen during the compression test, as shown in Fig. 2b. The sensor model is NANO-30, its frequency response range is 20–1200 kHz, and the sampling frequency is set to 1 MHz. Four acoustic emission probes are evenly arranged on the outer surface of the three-axis cavity, as shown in Fig. 2b. The contact part between the sensor and the triaxial cavity is coated with Vaseline to ensure its coupling effect. Through the AE timing characteristics and positioning information, the occurrence and development of micro-cracks in the specimen during the test are monitored, and the AR threshold value is set to 39 dB.

2.3. Scanning and characterization method of mortar-rock interface morphology

The JR-AF topography scanner is used to scan the three-dimensional morphology of the initial mortar-rock interface, as shown in Fig. 3a. The single-side scanning range of the scanning system is 100 mm × 75 mm, the measurement accuracy is ≤ ±0.03 mm, the resolution is 1280 pixels × 1024 pixels, and the average point distance is 0.06 mm. The binocular camera is used for non-contact scanning, and the single-side scanning time is less than 5 s. The scanned point cloud data is used to reconstruct the joint surface in three dimensions by triangular mesh, as shown in Fig. 3b. The height difference of the joint surface in the diagram is distinguished by color. With the height of the joint surface from high to low, the color gradually transitions from deep red to deep blue. The characteristic parameters of joint surface morphology are calculated by MATLAB software, The calculation method is as follows (Chen et al., 2010; Develi and Babadagli, 2015; Zhao et al., 2017):

The maximum absolute height S_p is the vertical distance between the highest peak and the deepest valley:

$$S_p = S_h + S_l \tag{1}$$

where S_h is the highest peak height, S_l is the lowest point height.

The root-mean-square (RMS) deviation of the surface S_q is the standard deviation of the height distribution:

$$S_q = \sqrt{\frac{1}{A}\iint z^2(x,y)\mathrm{d}x\mathrm{d}y} \tag{2}$$

where $z(x, y)$ is the height of the fracture surface at location (x, y); and A is the horizontal definition area, or the area of the rough surface projected onto the horizontal plane.

The arithmetic means height S_a is a parameter representing the mean surface roughness:

$$S_a = \frac{1}{A}\iint_A |z(xy)|\mathrm{d}x\mathrm{d}y \tag{3}$$

The skewness of the height distribution S_{sk} is used to quantify the symmetry of the height distribution of the joint surface.

$$S_{sk} = \frac{1}{S_q^3}\left(\frac{1}{A}\iint_A z^3(x,y)\mathrm{d}x\mathrm{d}y\right) \tag{4}$$

The kurtosis of the height distribution S_{ku} is used to quantify the flatness of the height distribution and indicates the concentration degree of the height distribution.

$$S_{ku} = \frac{1}{S_q^4}\left(\frac{1}{A}\iint_A z^4(x,y)\mathrm{d}x\mathrm{d}y\right) \tag{5}$$

The initial structural surface morphology parameters of the specimen are shown in Table 1.

(a) JR-AF Topography Scanner (b) Scanning image of initial structural plane morphology

Fig. 3. Three-dimensional scanning system and three-dimensional reconstruction image.

Table 1
The initial morphological parameters of the mortar-rock interface.

	S_p	S_a	S_q	S_{sk}	S_{ku}
Before test	4.305	1.107	1.291	−0.543	1.844

2.4. The strength parameters of mortar-rock composite specimens without bolts

A triaxial compression test was conducted on mortar-rock composite specimens without bolts, as illustrated in Fig. 4a. The deviatoric stress-strain curve is shown in Fig. 4b. With the increase of confining pressure, the curve types can be divided into two types: brittle curve and ductile curve. The confining pressure for the transformation from brittleness to ductility is between 15 MPa and 20 MPa. The compressive strength of the specimens is 65.96 MPa, 82.43 MPa, 95.91 MPa, and 115.21 MPa respectively under the four groups of confining pressures set in the test. According to the Coulomb strength criterion, the cohesion of the bolted mortar-rock composite specimen is 9.31 MPa, and the internal friction angle is 31.77°.

3. Results and discussion

3.1. Effect of bolt angle on the deviatoric stress-strain curve of mortar-rock composite materials

Fig. 5 illustrates the deviatoric stress-strain curves of mortar-rock composite specimens under four different confining pressures and various bolt inclination angles. Different bolt inclination angles change the mechanical properties of the specimen and change the yield platform. For confining pressures of 10 and 15 MPa, the peak stress points are marked with red dots on the curves. At higher confining pressures (20 and 25 MPa), the specimens exhibit plastic deformation after yielding, and thus no peak stress points are marked. When the confining pressure is 10 MPa, as the bolt inclination angle increases from small to large, the axial strains of the specimens at ultimate bearing capacity are 1.66%, 2.98%, 3.51%, 2.30%, 2.45%, and 2.33%, respectively. This indicates that with an increasing bolt inclination angle, the strain at peak stress first increases and then decreases. The maximum strain at peak stress occurs when the bolt inclination angle reaches 90°. It can be seen from the deviatoric stress-strain curve that the deformation of the specimen is small when it reaches the yield stress, and the curve is almost the same. At this moment, the specimen primarily undergoes elastic deformation, and its bearing capacity is jointly provided by the mortar-rock composite and the bolt. The axial strain of the specimen is the same when it enters the yield stage. When the specimen yields, the bolt acts, and different bolt angles change the size of the yield platform. When $\alpha = 90°$, the yield platform of the specimen is the largest. With the further increase or decrease of α angle, the yield platform of the specimen gradually decreases. After entering the residual stage, the specimen still has a large bearing capacity, which is different from the unbolted specimen. This phenomenon is more obvious when the confining pressure is lower than 20 MPa. With the increase of confining pressure, the yield platform of the specimen does not appear. With the continuous increase of axial strain, the bearing capacity of the specimen remains unchanged.

3.2. The effect of bolt angle on the mechanical characteristics of mortar-rock composite specimens

The compressive strength of mortar-rock composite specimens with different bolt angles under four groups of confining pressure is shown in Fig. 6a. Under the same confining pressure, with the increase of α angle, the compressive strength of the specimen increases first and then decreases. When the α angle is 90°, the compressive strength of the specimen is the largest. The strength of the specimen with α of 30° is higher than that of the specimen with α of 150°, the strength of the specimen with α of 60° is higher than that of the specimen with α of 120°, and the strength of the specimen with α of 135° is greater than that of the specimen with α of 150° but less than that of the specimen with α of 120°. With the increase of confining pressure, the compressive strength of specimens with α of 60°, 90°, and 120° tends to be equal. This indicates that when the bolt angle varies within a certain range, high confining pressure can mitigate the impact of different bolt angles on the compressive strength of the specimens.

To investigate the influence of bolt angles on the mechanical properties of mortar-rock composite specimens, the cohesion and internal friction angle of specimens with different bolt angles were calculated using the Coulomb criterion, as illustrated in Fig. 6b. With the increase of bolt angle α, the cohesion of mortar-rock composite specimens increases first and then decreases. When α is 90°, the cohesion of specimens is the largest. The maximum difference between the cohesion of the mortar-rock composite specimens with six anchor angles is 1.24 MPa, and the maximum difference between the internal friction angles is 0.59°.

According to the strength theory of a single structural plane estab-

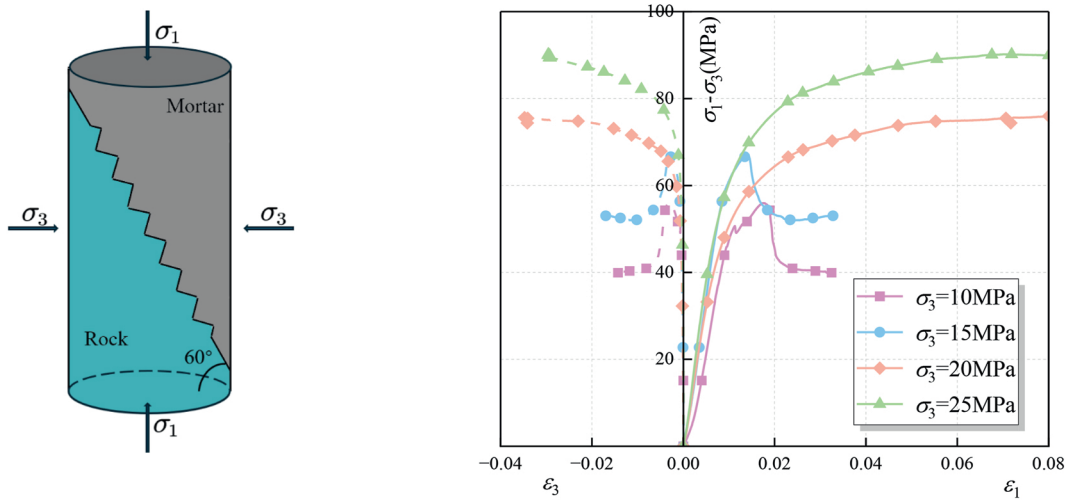

(a) Force diagram of a mortar-rock composite specimen (b) The deviatoric stress-strain curve of a boltless specimen

Fig. 4. Force diagram and deviatoric stress-strain curve of a mortar-rock composite specimen without bolt.

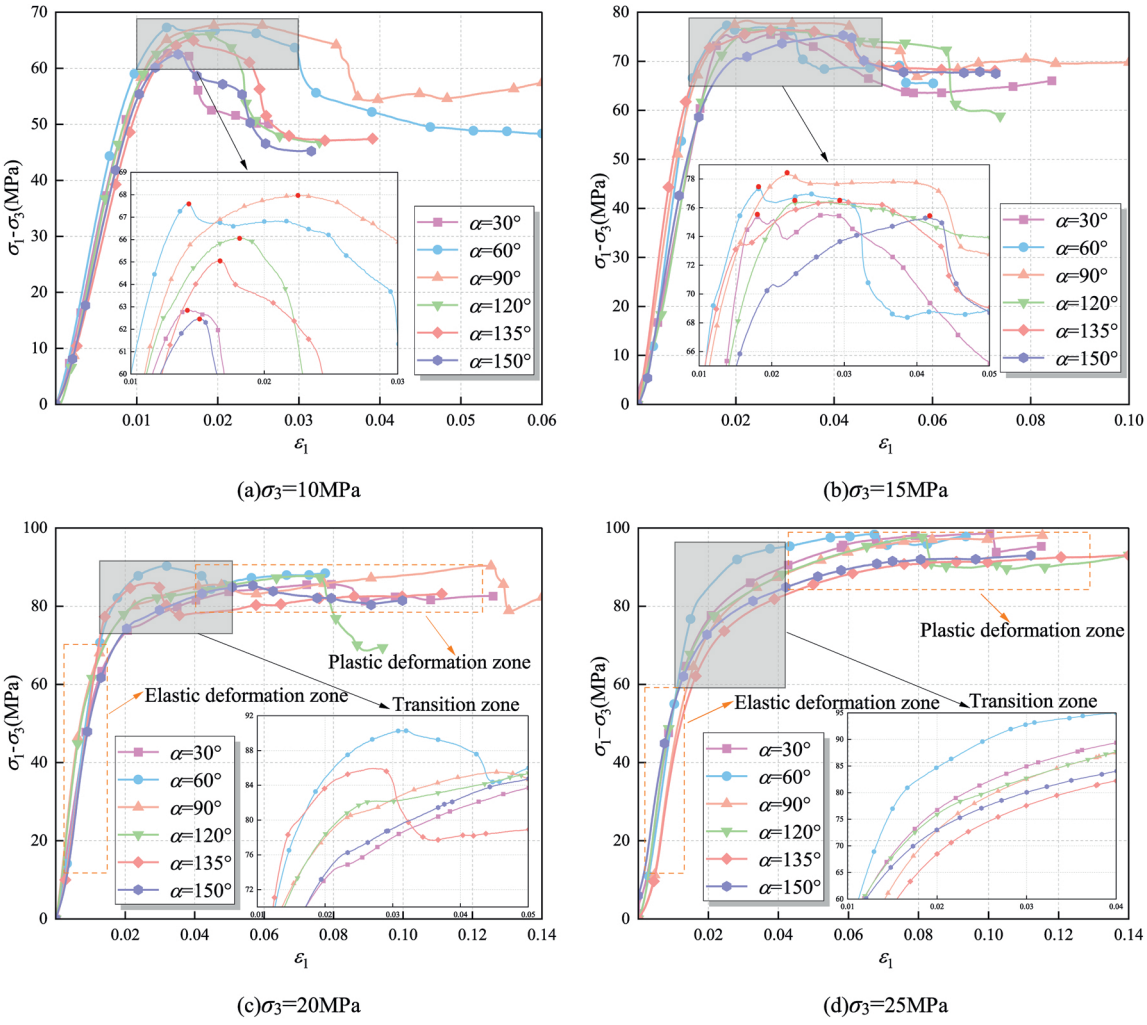

Fig. 5. The deviatoric stress-strain curves of mortar-rock composite specimens with different bolt angles.

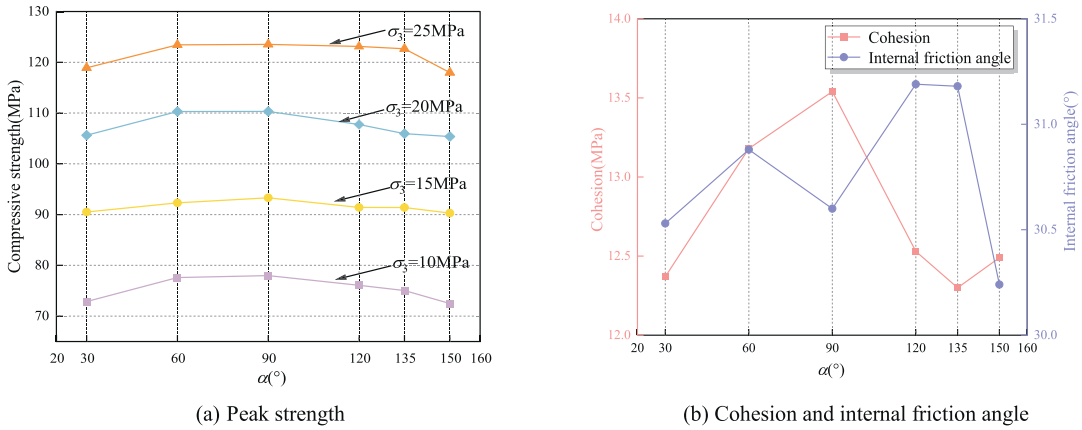

Fig. 6. Peak strength, cohesion, and internal friction angle of anchored mortar-rock composite specimens.

lished by Jeager, the normal stress (σ_n) and shear stress (τ) acting on the joint surface can be obtained by the maximum principal stress (σ_1) and the minimum principal stress (σ_3). The expression is as follows:

$$\begin{cases} \sigma_n = \dfrac{\sigma_1+\sigma_3}{2} + \dfrac{\sigma_1-\sigma_3}{2}\cos 2\beta \\ \tau = \dfrac{\sigma_1-\sigma_3}{2}\sin 2\beta \end{cases} \tag{6}$$

where β is the angle between the normal of a single joint surface and the maximum principal stress in the rock, based on this, the shear stress curves of mortar-rock composite specimens under six bolt angles are drawn, as shown in Fig. 7a. It can be seen from the curve that the bolt angle mainly changes the cohesion of the specimen, while the internal friction angle of the specimen is unaffected by it. Compared with the

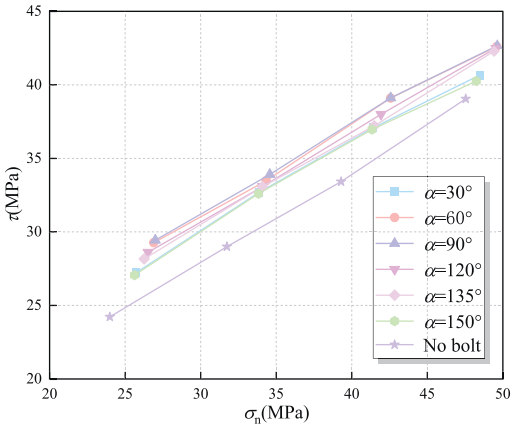

(a) Shear stress curve on the joint surface

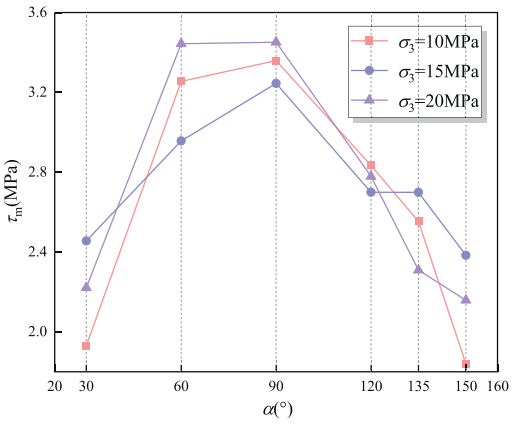

(b) The shear strength provided by the bolt to the structural plane

Fig. 7. Shear strength provided by different angle bolts.

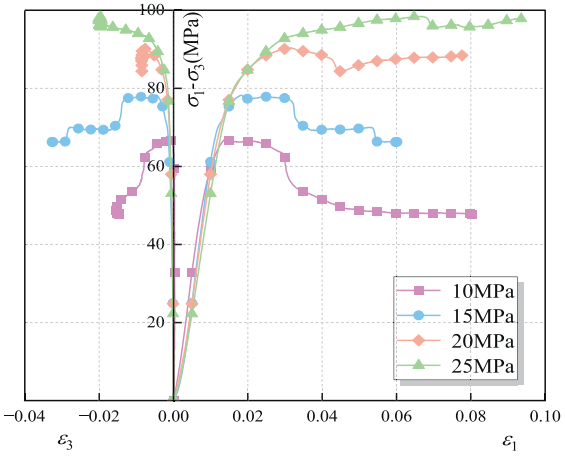

(a)The deviatoric stress-strain curves under different confining pressures

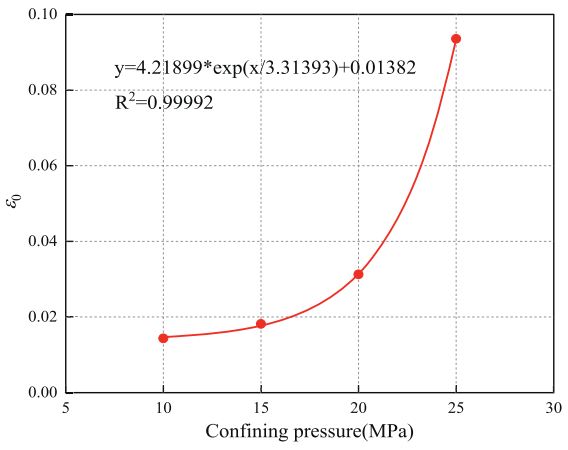

(b) Relationship between peak strain and confining pressure

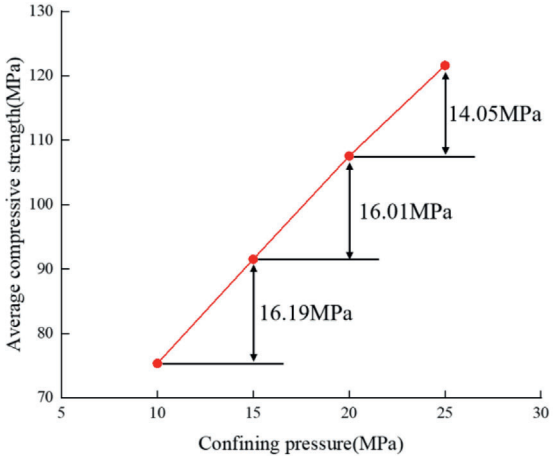

(c) Effect of confining pressure on compressive strength

Fig. 8. Effect of confining pressure on mechanical properties of mortar-rock composite specimens.

specimen without a bolt, the cohesion of the bolt specimen is significantly improved. To further analyze the influence of the angle of the bolt on the shear stress on the joint surface, the increase of the shear strength of the joint surface with different angles of the bolt is calculated, as shown in Fig. 7a. With the increase of bolt angle α, the shear strength provided by the bolt increases first and then decreases. When α is 90°, the shear strength provided is the largest. With the increase of confining pressure, this difference is limited.

3.3. *Effect of confining pressure on mechanical properties of mortar-rock mass specimens*

The change of confining pressure also affects the mechanical properties of the specimens. With the increase of confining pressure, the specimens with different bolt angles show similar properties. Therefore, the specimens with an bolt angle of 60° are selected for specific analysis. The deviatoric stress-strain curve is shown in Fig. 8a. With the increase of confining pressure, the yield stress and peak strength of the specimens increase gradually, and the post-peak curve changes from strain-softening to ideal plasticity. The confining pressure of the specimen from brittleness to plasticity is called the transformation pressure. When the confining pressure is lower than this strength, there is a peak point in the deviatoric stress-strain curve. When the confining pressure is higher than this strength, the deviatoric stress-strain curve does not peak. The increase in confining pressure enlarges the yield platform in the deviatoric stress-strain curve and improves the bearing capacity of the specimen. The strain when the specimen reaches the peak stress is affected by the confining pressure, as shown in Fig. 8b. The strain at the peak stress is exponentially related to the confining pressure, and the correlation coefficient is 0.99. Under four groups of confining pressures, the average compressive strength of specimens with different bolt inclination angles is counted. With the increase of confining pressure, the

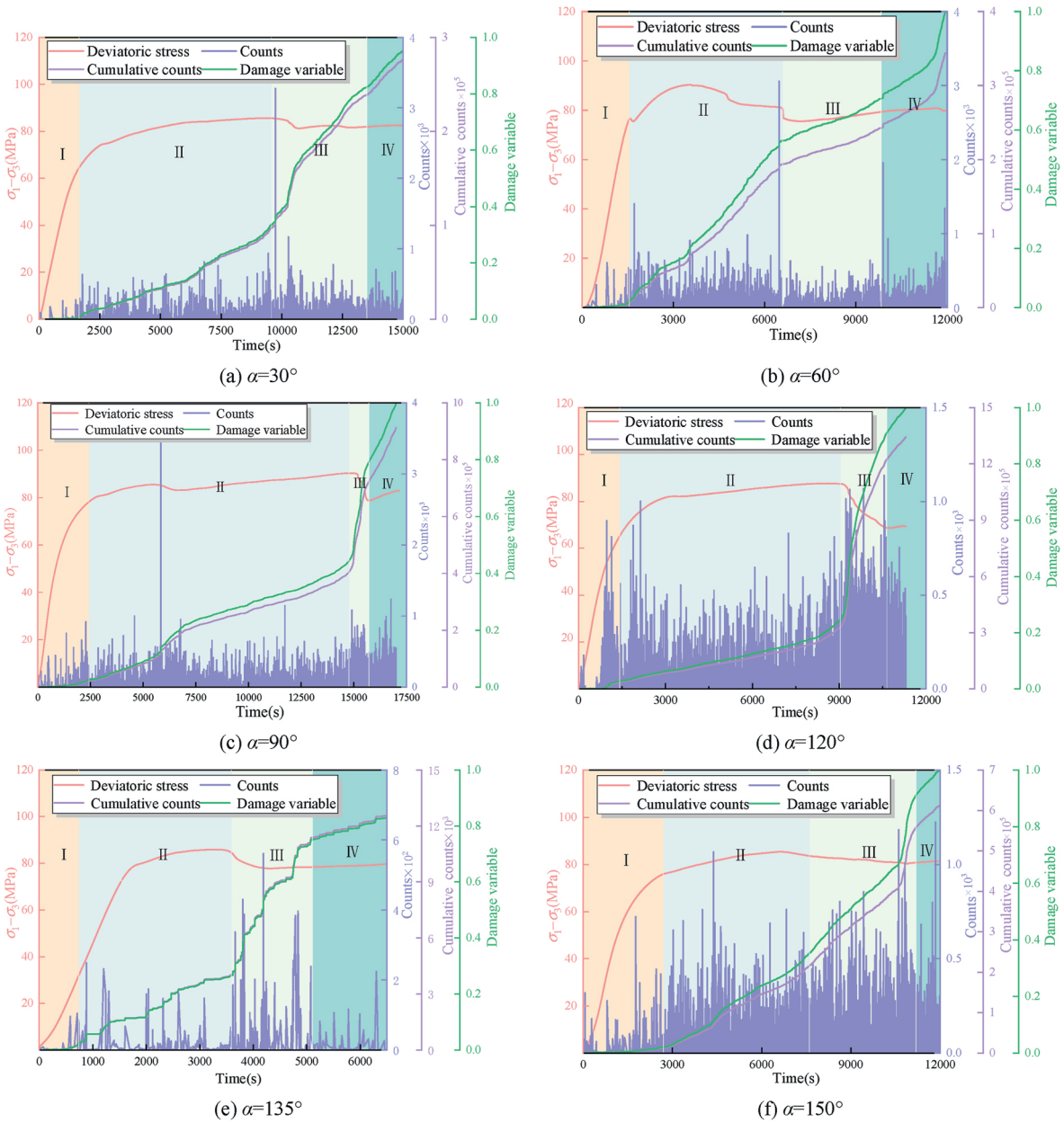

Fig. 9. Acoustic emission characteristic curve and damage variable curve.

increase of compressive strength gradually decreases, as shown in Fig. 8c.

3.4. Effect of bolt angle on acoustic emission characteristics of mortar-rock composite specimens

To explore the influence of different bolt angles on the acoustic emission characteristics during the compression test of the specimen, the relationship between the acoustic emission ringing count and the cumulative ringing count and time during the compression test was recorded when the confining pressure was 20 MPa, as shown in Fig. 9.

In the elastic stage, the deviatoric stress-strain curve of the specimen shows a linear relationship. The confining pressure is applied to the specimen before the axial loading, and the original cracks in the specimen are compacted, resulting in weak acoustic emission activity in this stage. The cumulative ringing count is approximately a horizontal line. After entering the yield stage, the new cracks in the specimen began to develop, the acoustic emission ringing count increased significantly, and the cumulative ringing count began to increase slowly. With further loading, the specimen enters the fracture stage, and the new cracks merge and penetrate, resulting in macroscopic fracture along the structural plane. The acoustic emission ringing count peaked at this time, and the cumulative ringing count growth rate has increased since then. After entering the stage of residual plastic flow, the specimen still has bearing capacity. With the increase of axial load, the specimen slides along the joint surface, and the cumulative ringing count growth rate slows down.

When $\alpha \leq 90°$, the specimen has an obvious ringing count peak during the compression test. With the increase of α angle, the time node of the peak ringing count is gradually advanced, and the time node of the peak ringing count corresponds to the stress drop time. When $\alpha > 90°$, the peak ringing count of the specimen during the compression test is no longer obvious, and the acoustic emission signal is denser when the stress drops.

The cumulative ring count of acoustic emission can better describe the damage characteristics of the specimen (Chen et al., 2017; Geng et al., 2017; Zhang et al., 2017), the relationship between the damage variable D and the cumulative ring count is expressed by Eq. (7). Assuming the cumulative acoustic emission ring count at complete failure of the intact material is C_0, and the cumulative ring count at a certain moment before failure is C_d. However, since the specimen still retains certain strength when the test is terminated, this study substitutes the final cumulative ring count at the end of the test for C_0.

$$D = \frac{C_d}{C_0} \tag{7}$$

Therefore, based on the correlation between the cumulative ring count and damage variable, the damage evolution process of the specimen can be divided into four stages. In the initial damage stage, the cumulative ringing count has almost no growth in the early stage of the test. In the stage of stable development of damage, the acoustic emission activity began to be active, and the cumulative ringing count began to increase steadily. In the stage of accelerated damage development, the cumulative ringing count in this stage increases sharply, the specimen breaks macroscopically, and the stress level drops. In the stage of damage and failure, the growth rate of cumulative ringing count in this stage begins to slow down, and the friction slip of the specimen along the structural plane will still produce a certain amount of acoustic emission activity. It can be seen from the cumulative ringing count curve that when α is 90°, the time point of the accelerated damage stage of the specimen is the latest. This bolt inclination angle can better control the development of cracks inside the specimen.

Table 2
Failure mode and bending degree of bolt.

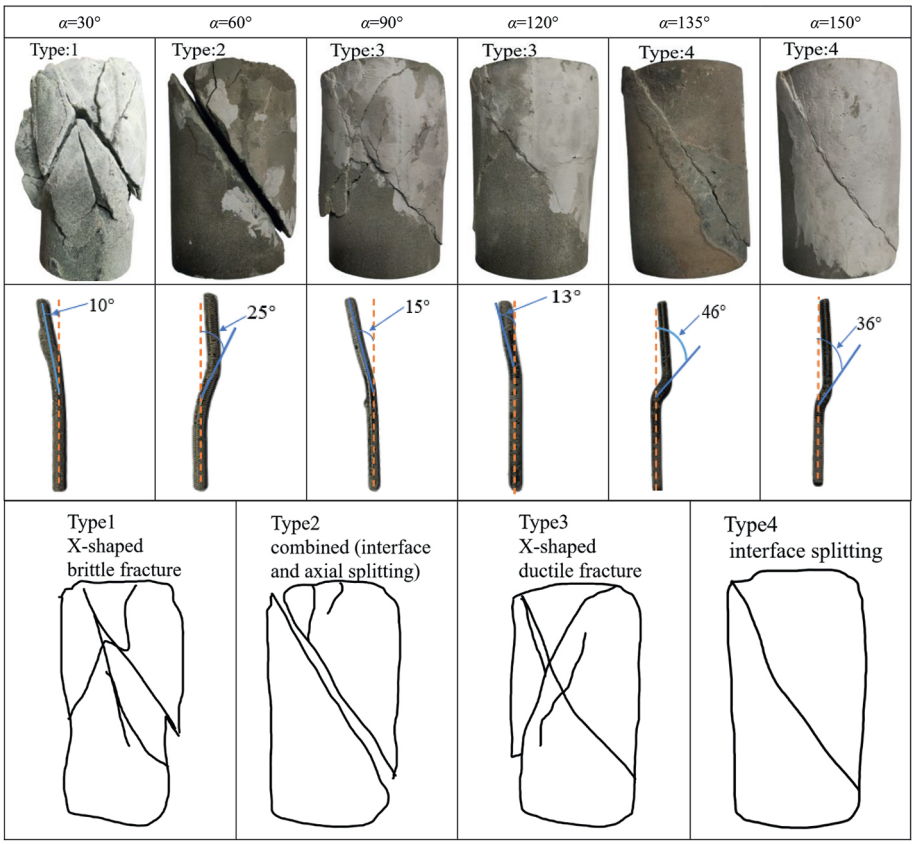

3.5. The failure modes of mortar-rock composite specimens with different bolt angles

Under the confining pressure of 20 ,MPa, four different failure modes were observed after triaxial compression tests on mortar-rock composite specimens with different bolt inclination angles. They are X-shaped brittle failure (Type 1), combined failure (Type 2), X-shaped ductile failure (Type 3), and structural plane failure (Type 4), as shown in Table 2. Among them, there are cracks along the structural plane and other macro cracks in the type 1 fracture. The overall plastic deformation of the specimen is not large, showing brittle failure and serious damage. In the type 2 fracture, there are penetrating cracks along the direction of the structural plane, but no cracks are running through the structural plane. The cracks only exist on the side of the mortar, and the mortar part produces large plastic deformation, while the rock part is intact, and the deformation is significantly smaller than the mortar part. In this case, the plastic deformation of the specimen is mainly produced by the mortar part. Type 3 fracture produces macroscopic fracture along the direction of the structural plane. The mortar part has a large plastic deformation, and the fracture runs through the structural plane, and the rock part also breaks. There is only macroscopic damage along the direction of the structural plane in the type 4 fracture. The two parts of the specimen slip along the structural plane, and the mortar part produces large plastic deformation without visible cracks. With the change of the bolt angle, the failure type of the specimen is also changing, and the angle of the bolt is directly related to the failure mode of the specimen. In this paper, the different failure modes of the specimen can be further explained by the cohesion of the specimen. Fig. 6b shows that the cohesion of the specimen changes with the angle of the bolt. When the cohesion of the specimen is large, the rock and mortar are crushed together on the structural surface to produce a type 3 fracture. When the cohesion begins to decrease, the rock part is not destroyed but only the mortar part has cracks. With further decrease of cohesion, the different angles of the bolt make the specimen produce two kinds of failure modes, one is a brittle fracture, and the other is that the mortar part does not produce visible cracks but only plastic deformation.

The different failure modes of the specimen also make the bending of the bolt inside the specimen different. Due to the brittle failure of the specimen with 30° α, there is no large slip along the joint surface, so the bending degree of the bolt is the smallest. The bending degree of the bolt increases when sliding along the joint surface because of the increase of the bolt angle of the specimen with α of 60°. With the further increase of α angle, the specimen produces type 3 damage, the mortar part produces large plastic deformation and produces macroscopic cracks along the direction of the bolt, which reduces the bending degree of the bolt. The specimen with α of 120° is the first to stop the compression test, so the bending degree of the bolt is the smallest. With the further increase of α angle, the specimen has type 4 of failure, and the specimen slides along the joint surface, so that the bending degree of the bolt is the largest among the four failure modes.

3.6. Effect of bolt angle on the morphological characteristics of joint plane

Table 3 shows the morphology diagrams of joint surfaces with different bolt inclination angles after the test. Considering the limitation of space, only the joint surface image of the specimen after the compression test is shown when the confining pressure is 15 MPa. By comparing the morphology images of the rock joint surface and mortar joint surface, it is found that the image of the rock joint surface is generally red, while the image of the mortar joint surface is mostly green and blue. This shows that when the specimen slides along the joint surface, the mortar joint surface is more serious than the rock joint surface. The serrations on the mortar joint surface are cut along the tooth root, and the serrations on the mortar joint surface fill the depression of the rock joint surface.

The three-dimensional laser scanning data of the joint surface after the compression test were statistically analyzed using the parameters described in Section 2.3 and the results are shown in Table 4. Among the parameters in Table 4, S_p, and S_a can be considered the main parameters that can effectively describe the joint surface roughness, with larger values indicating a rougher joint surface. Considering these two parameters, the mortar joint surface is the roughest when α is 90°, which is

Table 4
Structural surface morphology parameters.

α/°	Interface type	S_p/mm	S_a	S_q	S_{sk}	S_{ku}
30	mortar	5.507	0.402	0.572	−1.826	7.672
	rock	10.416	0.460	0.637	−0.769	5.377
60	mortar	4.950	0.499	0.713	−1.523	5.82
	rock	4.315	0.434	0.610	1.454	5.639
90	mortar	6.413	0.893	1.364	2.189	7.012
	rock	4.822	0.496	0.701	−1.696	6.465
120	mortar	4.958	0.516	0.633	−0.735	2.908
	rock	7.788	0.525	0.645	−1.179	3.851
135	mortar	7.579	0.691	0.924	0.251	4.377
	rock	8.246	0.735	1.027	−1.528	5.209
150	mortar	7.045	0.662	0.893	1.57	4.866
	rock	6.194	0.737	0.994	−1.096	5.416

Table 3
Reconstruction image of joint surface after test.

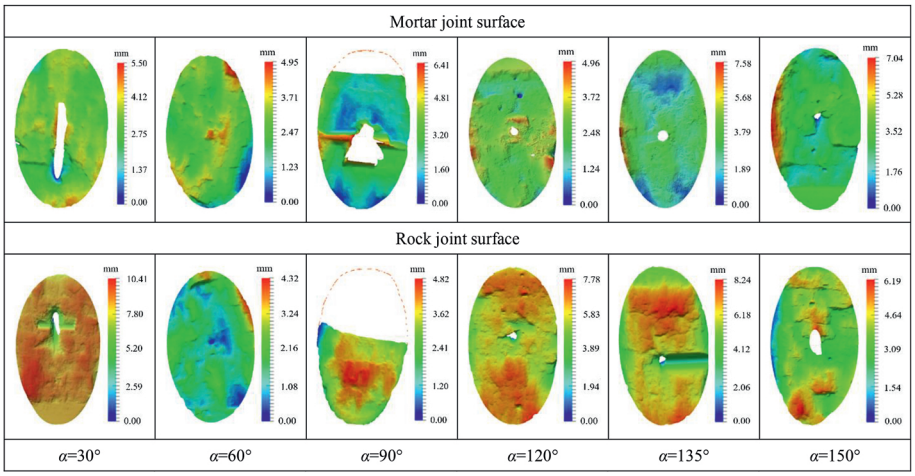

due to the different failure modes of the specimen. The joint surface when $\alpha > 90^\circ$ is generally rougher than that when $\alpha \leq 90^\circ$. A negative S_{sk} indicates that the joint surface has many deep and fine valleys. However, a positive S_{sk} indicates a joint surface with numerous peaks. When $S_{ku} < 3$, the height distribution is platykurtic and scattered. When $S_{ku} = 3$, the height distribution is normal. When $S_{ku} > 3$, the height distribution is leptokurtic and concentrated. With the increase of the bolt inclination angle α, the S_{sk} parameter of the mortar joint surface gradually changes from negative to positive, which indicates that the surface of the mortar joint surface changes from more depressions to more protrusions. The rock joint surface shows roughly the opposite properties. Except for the mortar joint surface when α is 120°, the S_{ku} parameters of the other joint surfaces are greater than 3. When $\alpha < 90^\circ$, the height distribution of the joint surface is leptokurtic and more concentrated. With the increase of α angle, the S_{ku} parameter of the mortar joint surface is gradually smaller than that of the rock joint surface. This shows that with the increase of α angle, the high concentration degree of rock joint surface is gradually greater than that of mortar joint surface.

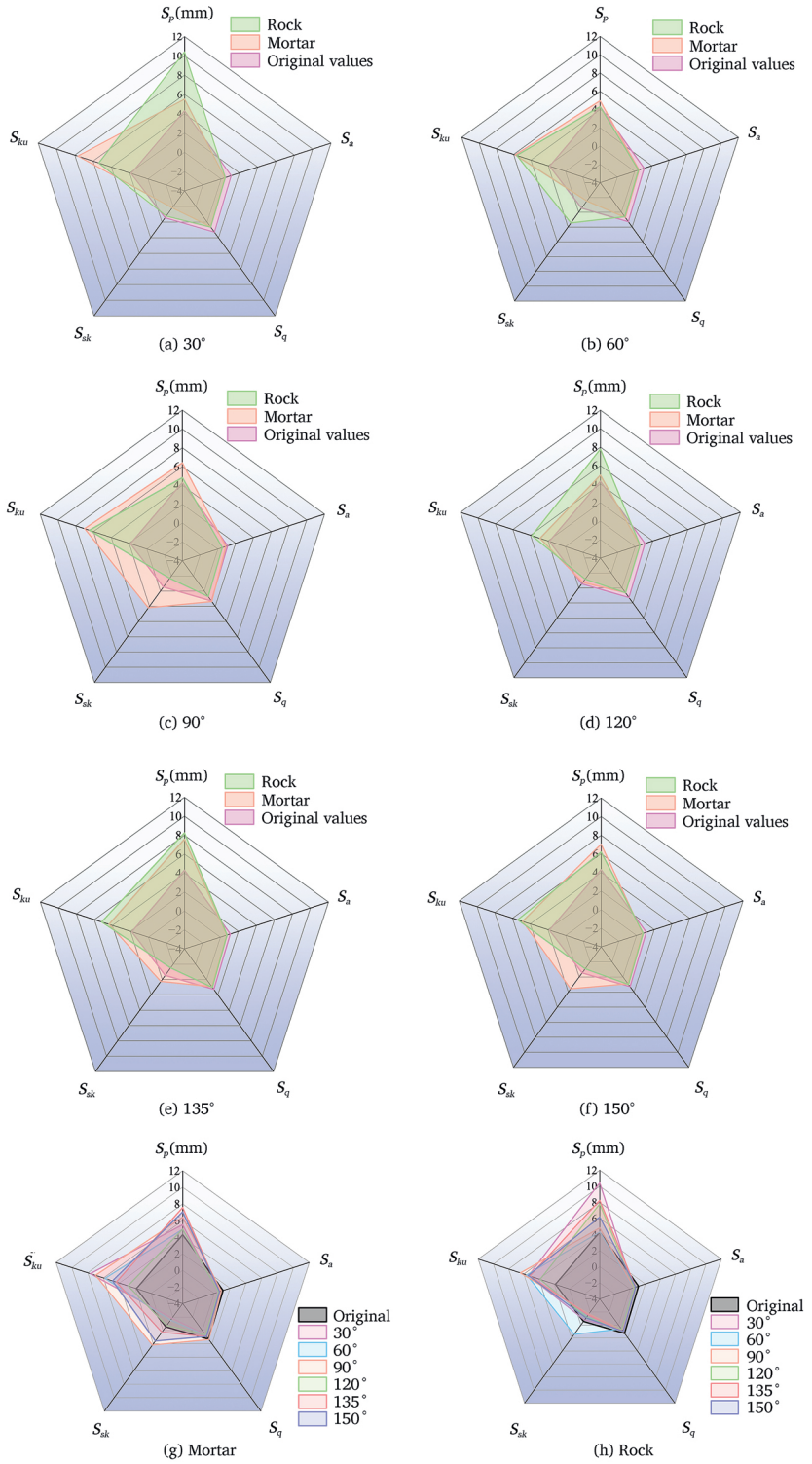

Fig. 10. Radar chart of joint surface morphological parameters under different bolt angles and media conditions.

To better demonstrate the variations in morphological parameters, they were plotted as a radar chart to highlight the differences in bolt angle parameters, as shown in Fig. 10. Fig. 10 comprises eight subplots displaying radar charts of morphological parameters for different bolt inclination angles ($\alpha = 30°$–$150°$) and interface types (mortar/rock). In the first six subplots, orange polylines represent mortar interfaces while green polylines denote rock interfaces. The protruding directions of the pentagon indicate the dominant parameters, with larger areas indicating greater interface roughness. Protruding axes identify dominant parameters, revealing the nonlinear influence of bolt inclination angle on roughness. At $\alpha = 90°$, the orange pentagon exhibits pronounced protrusions along the S_a and S_q axes, resulting in the largest polygon area – confirming the highest S_a value for mortar at this bolt inclination angle. Comparative analysis of small bolt inclination angles ($\alpha \leq 90°$) versus large angles ($\alpha > 90°$) reveals: At $\alpha = 30°$ (Fig. 10a), the orange mortar interface exhibits severely recessed S_a-axis while the green rock interface shows prominently protruded S_p-axis, aligning with Type I brittle failure. At $\alpha = 150°$ (Fig. 10f), moderate protrusions along the mortar S_a and S_q axes correspond to Type IV sliding failure – interface-dominated. The evolution of height distribution demonstrates a polarity reversal in skewness (S_{sk}): The orange mortar interface shifts from negative extremes at $\alpha = 30°$ through peak positive skewness at $\alpha = 90°$ to positive values at $\alpha = 150°$—aligning with the ductile failure mechanism where mortar protrusions fill rock grooves. In contrast, the green rock interface exhibits predominantly negative skewness except at $\alpha = 60°$.The kurtosis parameter (S_{ku}) exhibits a concentration effect, where the orange mortar interface shows S_{ku} decreasing from 7.672 at $\alpha = 30°$ (indicating intense concentration with sharp polyline spikes) to 2.908 at $\alpha = 120°$ (reflecting dispersed distribution with contracted profile). This suggests that height concentration ($S_{ku} > 3$) at small bolt inclination angles may intensify local stress concentration, potentially triggering brittle failure. Simultaneously, the radar charts reveal asymmetric evolution between interfaces with roughness reversal: mortar polygonal areas are generally smaller than rock at $\alpha \leq 90°$, but overtake rock surfaces at $\alpha > 90°$.

Fig. 11 shows the variation of joint surface morphology parameters before and after the compression test ($\Delta S = S_{after} - S_{before}$). The joint surface of rock and mortar shows the same change rule. It is found that after the test, the S_p parameters of all joint surfaces are larger than those before the test, which indicates that the distance between the highest point and the lowest point of the joint surface increases. The S_a parameters after the compression test are all reduced, which indicates that the roughness of the joint surface is reduced and the serrations on the joint surface are smoothed. The S_q parameter also shows the same conclusion. The increase of S_{ku} parameter indicates that the height distribution of the joint surface becomes concentrated after the test.

4. Strength prediction model

It is assumed that the shear strength of structural planes conforms to the Coulomb criterion:

$$\tau = \sigma \tan \varphi + c \tag{8}$$

The conditions of shear failure along the structural plane can be obtained by combining the two Eqs. (6) and (7).

$$\sigma_1 - \sigma_3 = \frac{2(c + \sigma_3 \tan \varphi)}{(1 - \tan \varphi \cot \beta)\sin 2\beta} \tag{9}$$

where c is the cohesion of the structural plane, and φ is the internal friction angle of the structural plane.

The shear strength of the anchored joint surface is provided by the joint surface and the bolt (Lin et al., 2022):

$$\tau = \tau_j + \tau_z + \tau_h \tag{10}$$

where τ_j is the shear strength of the structural plane, τ_z is the shear strength provided for the axial force of the bolt, τ_h is the shear strength provided for the transverse shear force of the bolt.

The expression of each shear component in the above formula is:

$$\begin{cases} \tau_j = \sigma \tan(\varphi + \psi_j) + c \\ \tau_z = \dfrac{N}{A_e}\left[\sin\alpha \tan(\varphi + \psi_j) + \cos\alpha\right] \\ \tau_h = \dfrac{Q}{A_e}\left[\sin\alpha - \cos\alpha \tan(\varphi + \psi_j)\right] \end{cases} \tag{11}$$

where ψ_j is he dilatancy angle of structural plane, N is the axial force when the bolt yield, Q is the shear force when the anchor yield,α is the angle between bolt and structural plane, A_e is the equivalent shear area of the bolt.

From the above formula, the compressive strength of mortar-rock composite specimens with different bolt angles under three-dimensional stress can be obtained:

$$\begin{aligned} \sigma_1 - \sigma_3 = {} & \frac{2\left[c + \sigma_3 \tan(\varphi + \psi_j)\right]}{(1 - \tan\varphi \cot\beta)\sin 2\beta} + \frac{2\frac{N}{A_e}\left[\sin\alpha \tan(\varphi + \psi_j) + \cos\alpha\right]}{(1 - \tan\varphi \cot\beta)\sin 2\beta} \\ & + \frac{2\frac{Q}{A_e}\left[\sin\alpha - \cos\alpha \tan(\varphi + \psi_j)\right]}{(1 - \tan\varphi \cot\beta)\sin 2\beta} \end{aligned} \tag{12}$$

Because in the triaxial compression state, it is difficult for the specimen to undergo dilatancy when shear failure occurs along the joint surface, the above formula can be further simplified as:

$$\begin{aligned} \sigma_1 - \sigma_3 = {} & \\ & = \frac{2[c + \sigma_3 \tan\varphi]}{(1 - \tan\varphi \cot\beta)\sin 2\beta} + \frac{2\frac{N}{A_e}[\sin\alpha \tan\varphi + \cos\alpha]}{(1 - \tan\varphi \cot\beta)\sin 2\beta} \\ & + \frac{2\frac{Q}{A_e}[\sin\alpha - \cos\alpha \tan\varphi]}{(1 - \tan\varphi \cot\beta)\sin 2\beta} \end{aligned} \tag{13}$$

The following assumptions are made for the test results: under the same bolt angle, the axial force, shear force, and equivalent shear area of the bolt are the same when the bolt yields. Therefore, N/A_e and Q/A_e are considered as a whole calculation. Two sets of auxiliary experiments are set up to solve the values of N/A_e, Q/A_e. The test is as follows: Select the same material to make the test piece, only change the regular sawtooth fluctuation angle on the structural surface, set it to 30° and 60°, do not use the anchor bolt, and carry out the triaxial compression test under the same four groups of confining pressure. The deviatoric stress-strain curve is shown on Fig. 12. The cohesion of the specimen with the undulation angle of 30° is 9.49 MPa and the internal friction angle is 30.81°. The cohesion of the specimen with a joint surface undulation angle of 60° is 9.76 MPa, and the internal friction angle is 32.17°. Due to the limitation of test conditions, this paper only predicts the strength of the specimen when $\alpha = 90°$. The same bolt with $\alpha = 90°$ was used to anchor the above two specimens, and the deviatoric stress-strain curve and compressive strength of the two specimens were obtained by triaxial compression test under the same confining pressure of four groups, as shown in Fig. 13. The above parameters are brought into the Eq. (12) to solve the N/A_e and Q/A_e values provided by the anchor rod when $\alpha = 90°$ under different confining pressures, as shown in Table 5. These values represent numerical solutions obtained by solving for undetermined coefficients in the equations. Their actual physical meaning should be interpreted by considering the two parameters in the table as an integrated system. The holistic analysis yields positive results, indicating that the rock bolts provide a reinforcing effect on the compressive strength of the anchored rock mass. The following table parameters are substituted into Eq. (12) to solve the triaxial compressive strength of the specimen when $\alpha = 90°$ and the undulation angle of the joint surface is 45°, as shown in Fig. 14. The maximum error between the predicted value and the experimental value of the compressive strength is 9.50% when the confining pressure is 10 MPa. The minimum error occurs when the confining pressure is 15 MPa, and the error is 3.39%. The overall average error under four groups of confining pressures is 6.24%. This

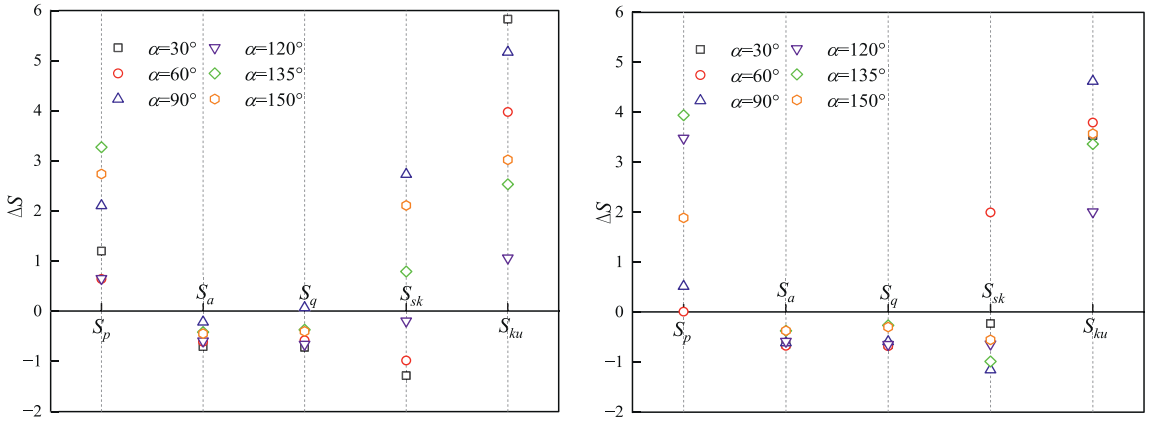

(a) Mortar joint surface (b) Rock joint surface

Fig. 11. Changes of morphological parameters of mortar and rock joint surface before and after test.

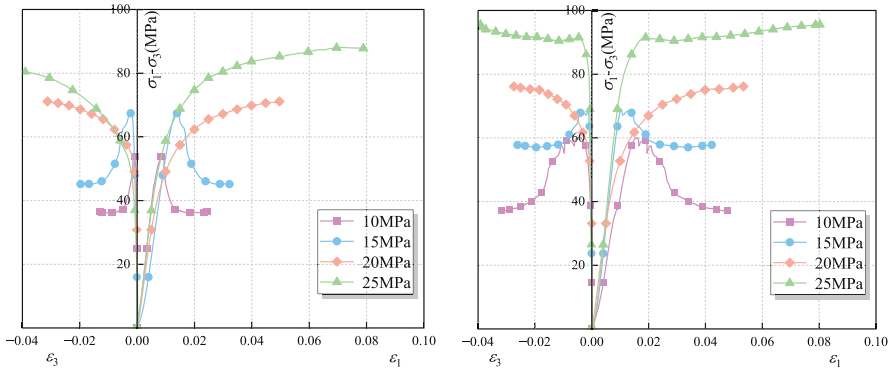

(a) The undulating angle is 30° (b) The undulating angle is 60°

Fig. .12. The deviatoric stress-strain curves of specimens with 30° and 60° undulating angles of structural planes are obtained.

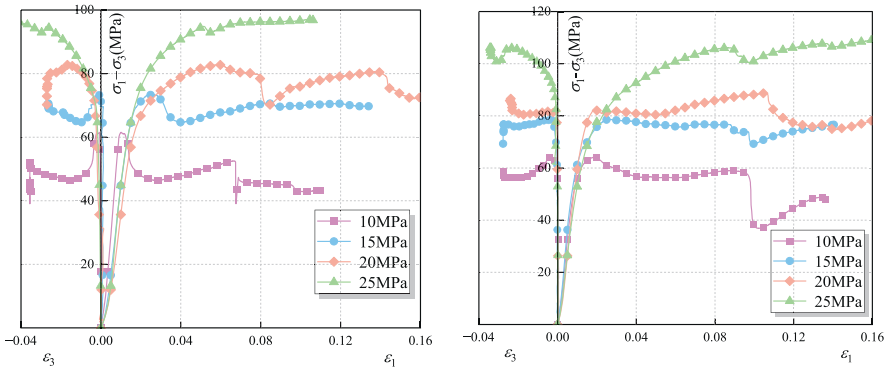

(a) The undulating angle is 30° (b) The undulating angle is 60°

Fig. 13. The deviatoric stress-strain curves of bolt specimens with structural plane undulation angles of 30° and 60°.

Table 5
Shear strength provided by bolts to structural plane.

Confining pressure/MPa	N/A_e/MPa	Q/A_e/MPa
10	−22.11	17.22
15	7.373	0.37
20	2.62	2.608
25	122.63	−66.85

prediction model can predict the compressive strength of anchored joint specimens under different confining pressures and has high reliability. The validity of the hypothesis has been substantiated, confirming that under identical bolt inclination angles, the axial force, shear force, and equivalent shear area of the rock bolt at yielding remain consistent. The compressive strength of the bolted specimen is jointly governed by the interfacial bond strength and the mechanical contribution of the rock bolt. Notably, when the roughness of the structural plane is altered while maintaining constant anchoring conditions, the compressive resistance provided by the rock bolt exhibits minimal variation. Based on the

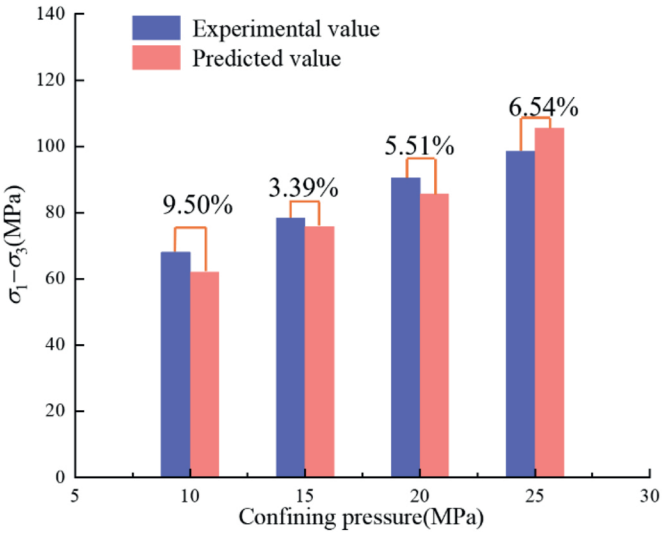

Fig. 14. Comparison of predicted values and experimental values.

experimental methodology and theoretical assumptions presented in this study, it can be reasonably deduced that the proposed strength model retains its applicability across varying bolt inclination angles.

5. Discussion

5.1. Construction feasibility

Although experimental data indicate optimal mechanical performance within the 60°–120° bolt inclination angle range, underground engineering requires a holistic design approach that integrates drilling accessibility and spatial geometric constraints. The actual angular control accuracy of bolt drilling machines in coal mine roadways typically maintains a range of ±5°. Although the 90° bolt inclination angle recommended in this study can be readily achieved during roof construction, rib-side installation is often constrained to 60°–70° due to dimensional limitations of drilling equipment. Our research demonstrates that when the bolt inclination angle varies within 90° ± 30°, the bolted specimens exhibit minimal strength reduction below 2.43% across four different confining pressure conditions, with this strength discrepancy progressively diminishing as confining pressure increases. Significantly, exceeding the 90° ± 30° angular range leads to substantially greater strength reductions, with specimens at 30° showing an average 4.38% strength decrease compared to 90° bolted specimens, while those at 150° demonstrate a 4.81% reduction. These results confirm that optimal anchoring performance can be reliably achieved within the 90° ± 30° range for the rock bolt to rock-mortar interface angle.

5.2. Geological compatibility

For stratified rock masses, bolts should be preferentially installed perpendicular to bedding planes (i.e., 90°) to maximize interlayer shear resistance. However, in steeply dipping jointed zones, the angle may need to be adjusted to approximately 60° or 120° to intersect more joints and activate their shear contribution. In high-stress zones, bolt inclination angles that induce ductile failure modes (i.e., 90° and 120°) should be prioritized to accommodate large deformations through coordinated load-bearing. The failure type can serve as an engineering warning indicator—if Type 1 (brittle) failure occurs in the field, the bolt angle requires adjustment.

5.3. Study limitations

In this study, the 60° inclined specimens were prepared with both ends of the rock bolts positioned at the specimen surfaces. Due to the significant stiffness contrast between the steel bolts and the mortar-rock composite material, stress concentration may occur during confining pressure loading, potentially leading to deformation incompatibility in the anchorage zone. This condition could result in non-uniform stress transfer into the specimen interior, while the effect of mortar-filled gaps between drill holes and bolts on stiffness discontinuity requires further verification from perspectives of micromechanics and load transfer mechanisms.

It should be noted that the consistent mortar-filling technique employed in specimen preparation ensured the bolt inclination angle as the sole controlled variable. Acoustic emission monitoring during confining pressure application revealed that the distinctive geometric configuration of 60° inclined specimens did not induce microcracks attributable to stress concentration around the bolts. Although stiffness mismatch may cause localized pressure inhomogeneity, the overall stress path remains valid for characterizing triaxial compression behavior. Future research should employ advanced techniques such as distributed optical fiber sensing to directly measure actual confining pressure distribution across structural planes.

6. Conclusion

This study systematically investigates the influence of bolt angles and confining pressure on mechanical properties and failure mechanisms of mortar-rock composite specimens through triaxial compression tests. Key conclusions are summarized as follows:

1. The bolt angle significantly influences the strength and ductility of mortar-rock composite specimens. Specimens with a 90° bolt angle exhibit the maximum compressive strength and the highest ductility. While increasing confining pressure enhances the ductility of the anchored composite material, it concurrently diminishes the effect of the bolt angle.
2. For mortar-rock composite specimens with bolt angles $\leq$ 90°, the peak acoustic emission (AE) ringing counts synchronize with stress drops. However, when the bolt angle exceeds 90°, the peak AE ringing count signals are no longer detectable. Cumulative AE ringing counts effectively characterize damage evolution. Specimens with a 90° bolt angle exhibit the latest stage of accelerated damage and demonstrate optimal load-bearing performance.
3. Three-dimensional reconstruction reveals that during shear-sliding failure, the serrated roots on the mortar interface undergo shear cutting, while the convex portions fill the rock grooves. As the bolt angle increases, the roughness of the failure surface progressively increases, yet it remains lower than the initial state.
4. The bolt angle induces four distinct failure modes in mortar-rock composite specimens. It is recommended to prioritize the use of bolt angles (90°–120°) associated with ductile failure to enhance load-bearing capacity.
5. The proposed triaxial compressive strength prediction model demonstrates good agreement with experimental data in predicting the strength of mortar-rock composite specimens. The maximum prediction error of 9.50% occurs under a confining pressure of 10 MPa, while the minimum error of 3.39% is observed at a confining pressure of 15 MPa. The average prediction error across the four sets of confining pressures is 6.24%.

CRediT authorship contribution statement

Minzhen Zhang: Writing – review & editing, Writing – original draft, Resources, Formal analysis, Data curation. **Yanlin Zhao:** Visualization, Validation, Supervision, Funding acquisition. **Wenyu Tang:**

Supervision, Investigation. **Rui Luo:** Software, Data curation. **Tianyao Li:** Resources, Formal analysis. **Ximing Luo:** Formal analysis, Data curation.

Declaration of competing interest

The authors declare that they have no known competing financial interests or personal relationships that could have appeared to influence the work reported in this paper.

Acknowledgments

This work was financially supported by the National Natural Science Foundation of China (grant number 52274118, 52574143).

References

Chen, S., Yang, C., Wang, G., 2017. Evolution of thermal damage and permeability of Beishan granite. Appl. Therm. Eng. 110, 1533–1542.

Chen, Y., Cao, P., Chen, R., Teng, Y., 2010. Effect of water–rock interaction on the morphology of a rock surface. Int. J. Rock Mech. Min. Sci. 47, 816–822.

Chen, Y., Li, C.C., 2015. Performance of fully encapsulated rebar bolts and D-Bolts under combined pull-and-shear loading. Tunn. Undergr. Space Technol. 45, 99–106.

Chen, Y., Yang, J., Li, M., Zhou, L., Guo, B., Zuo, J., 2023. Effects of roughness on shear properties and acoustic emission characteristics of bonded rock-concrete interfaces. Constr. Build. Mater. 398, 132405.

Develi, K., Babadagli, T., 2015. Experimental and visual analysis of single-phase flow through rough fracture replicas. Int. J. Rock Mech. Min. Sci. 73, 139–155.

Feng, J., Chen, J., Wang, D., 2025. Research on direct shear tests and calculation methods for BFRP anchor rods reinforcing rock joint surfaces. Rock Mech. Rock Eng. 1–16.

Fu, J., Sarfarazi, V., Haeri, H., Zarei, A.S., Bahrami, R., Imani, M., Marji, M.F., 2024. Experimental and numerical analyses of shear failure mechanisms of rock bolt surrounded by bedded rock. Int. J. GeoMech. 24, 24.

Geng, J., Sun, Q., Zhang, Y., Cao, L., Zhang, W., 2017. Studying the dynamic damage failure of concrete based on acoustic emission. Constr. Build. Mater. 149, 9–16.

Gregor, P., Mirzaghorbanali, A., McDougall, K., Aziz, N., Jodeiri Shokri, B., 2023. Shear behaviour of fibreglass rock bolts for various pretension loads. Rock Mech. Rock Eng. 56, 8083–8113.

Li, Y., Liu, C., 2019. Experimental study on the shear behavior of fully grouted bolts. Constr. Build. Mater. 223, 1123–1134.

Liao, P., An, Z., Wang, F., Guo, C., Yao, H., Bai, D., 2025. Influence of normal stress on the shear failure mechanisms of cement-rock composites. Constr. Build. Mater. 470, 140553.

Lin, H., Sun, P., Chen, Y., Zhu, Y., Fan, X., Zhao, Y., 2022. Analytical and experimental analysis of the shear strength of bolted saw-tooth joints. European J. Environ, Civil Eng. 26, 1639–1653.

Liu, J., Zeng, X., Zheng, W., Lai, H., Wang, Y., Wang, F., Qiu, H., 2025. Dynamic behavior of a running crack crossing mortar-granite interface with different interface inclinations. Eng. Fract. Mech. 314, 110705.

Maiolino, O.S., Pellet, F.L., 2015. Full scale lab testing for the determination of rock bolt contribution to reinforced joint shear strength. ISRM Congress 2015, Proceedings of the International Symposium on Rock Mechanics, p. 1e9.

Pinazzi, P., Spearing, A.S., Jessu, K., Singh, P., Hawker, R., 2020. Mechanical performance of rock bolts under combined load conditions. Int. J. Min. Sci. Technol. 30, 167–177.

Renaud, S., Bouaanani, N., Miquel, B., 2021. Experimental, analytical, and finite element assessment of the shear strength of concrete-rock interfaces at different scales. Int. J. Numer. Anal. Methods GeoMech. 45, 1238–1259.

Selçuk, L., Aşma, D., 2019. Experimental investigation of the rock–concrete bi materials influence of inclined interface on strength and failure behavior. Int. J. Rock Mech. Min. Sci. 123, 104119.

Shan, R., Liu, N., Sun, P., Zhao, Z., Dong, R., Dou, H., Meng, H., Bai, Y., 2025. Experimental and numerical simulation study of rough jointed rock samples under triaxial compression conditions. Eng. Fract. Mech. 314, 110707.

Terron-Almenara, J., Holter, K.G., Jakobsen, P.D., Aagaard, B., Lund, A.K., 2025. Permanent tunnel support with reinforced shotcrete arches and forepoling in over-consolidated till and weathered rock. A case study based on the construction of the Bergås tunnel, Norway. Tunn. Undergr. Space Technol. 157, 106256.

Wang, W., Le, P., Liu, S.-f., Cao, Y.-j., Mei, Z.-p., Zhu, Q.-z., 2025. Experimental study on mechanical properties and brittleness of sandstone-concrete combined body under triaxial seepage-stress coupling. Constr. Build. Mater. 465, 140016.

Wang, W., Yang, X., Huang, S., Yin, D., Liu, G., 2020. Experimental study on the shear behavior of the bonding interface between sandstone and cement mortar under freeze–thaw. Rock Mech. Rock Eng. 53, 881–907.

Weilv, W., Xu, W., Jianpin, Z., 2021. Effect of inclined interface angle on shear strength and deformation response of cemented paste backfill-rock under triaxial compression. Constr. Build. Mater. 279, 122478.

Wu, G., Yu, W., Zuo, J., Du, S., 2020. Experimental and theoretical investigation on mechanisms performance of the rock-coal-bolt (RCB) composite system. Int. J. Min. Sci. Technol. 30, 759–768.

Xue, F., Tong, Z., Chen, W., Wang, T., You, X., Lin, Z., 2025. Experimental study on anchorage mechanical effect of rock bolts on cross-jointed rock mass using DIC and AE. Theor. Appl. Fract. Mech., 104875

Yang, J., Li, Z., He, X., Zhao, Y., Sun, Z., Wang, Z., Bian, W., 2024. Comparative analysis of the performance of Thin Spray-on liner with shotcrete and mesh support. Constr. Build. Mater. 455, 139195.

Yu, W., Wu, G., Pan, B., Wu, Q., Liao, Z., 2021. Experimental investigation of the mechanical properties of sandstone–coal–bolt specimens with different angles under conventional triaxial compression. Int. J. GeoMech. 21, 04021067.

Yuan, S., Du, B., Shen, M., 2024. Experimental and numerical investigation of the mechanical properties and energy evolution of sandstone–concrete combined body. Sci. Rep. 14.

Zheng, H.F., Jiang, Y.J., Wu, X.Z., Zhang, S.H., Sugimoto, S., 2025. Investigation on stress distribution and prestress loss model of prestressed anchor cables considering corrosion-induced debonding. Rock Mech. Bull. 4, 100189.

Zhang, F., Cheng, T., Zhu, Z., Hu, D. & Shao, J. The effect of pre-heating treatment and water–cement ratio on the shearing behavior and permeability of granite–cement interface samples. Rock Mech. Rock Eng., 1-12.

Zang, H.Z., Wang, S.Y., 2026. Recent advancements for cement grout diffusion mechanisms within rock fractures. Rock Mech. Bull. 5, 100237.

Zhang, S., Jiang, Y., Luan, H., Li, B., Liu, J., Wang, C., 2024a. Study on shear mechanical characteristics of rock joints under different Anchorage lengths. Rock Mech. Rock Eng. 57, 9959–9981.

Zhang, S., Wang, C., Wang, G., Zheng, X., Guan, H., Liu, T., Xu, F., 2023. Experimental and numerical study on shear behaviors of rock joints reinforced by SFCBs and BFRP bars. Rock Mech. Rock Eng. 56, 1717–1737.

Zhang, X., Lu, Y., Tang, J., Zhou, Z., Liao, Y., 2017. Experimental study on fracture initiation and propagation in shale using supercritical carbon dioxide fracturing. Fuel 190, 370–378.

Zhang, X., Yao, W., Wang, X., Li, W., Zhu, X., Huang, H., 2024b. Experimental study on mechanical properties of low-strength mortar–granite composite specimens. Rock Mech. Rock Eng. 1–16.

Zhao, Y., Shen, M., Bi, J., Wang, C., Yang, Y., Du, B., Ning, L., 2022. Experimental study on physical and mechanical characteristics of rock-concrete combined body under complex stress conditions. Constr. Build. Mater. 324, 126647.

Zhao, Y., Zhang, L., Wang, W., Tang, J., Lin, H., Wan, W., 2017. Transient pulse test and morphological analysis of single rock fractures. Int. J. Rock Mech. Min. Sci. 91, 139–154.